



Effect of Al content on thermal stability, shape memory effect and mechanical properties of Cu–Al–Fe shape memory alloys

Yunpeng Gao¹ · Jiaying Jian¹ · Zengyun Jian¹

Received: 26 November 2023 / Accepted: 25 April 2024 / Published online: 23 May 2024
© Akadémiai Kiadó, Budapest, Hungary 2024

Abstract

Cu–Al–Fe shape memory alloys are a new kind of smart materials with high phase transition temperature. However, poor thermal stability and poor shape memory effect limit the commercial application range. In this paper, the effect of Al content on microstructure, thermal stability, shape memory effect and mechanical properties of Cu–Al–Fe shape memory alloys was investigated systematically by changing Al content, so as to obtain the optimal composition ratio for better commercial application. The results show that in the as-cast state, the microstructure is a mixture of (Cu) phase, β' martensite and Fe(Cu, Al) phase with Al content of 11 mass%, and a mixture of β' martensite and Fe(Cu, Al) phase with Al content of 12 mass% and 13 mass%. After quenching, β' martensite exists in all alloys, while (Cu) phase and Fe(Cu, Al) phase disappear, and γ' martensite also exists at Al content of 13 mass%. The shape memory alloy effect of as-cast alloy is enhanced with the increase of Al content, while the shape memory effect of quenched alloy increases first and then decreases. Among them, Cu₈₂Al₁₃Fe₅ has the best shape memory effect, the recovery ratio reaches 84.38%, and it also has the best thermal stability.

Keywords Cu–Al–Fe · Microstructure · Martensite · Shape memory effect

Introduction

Shape memory alloys (SMAs) have been used widely in sectors of weapon-equipment, biomedicine and aero-space due to their unique shape memory effect (SME) [1–3]. Currently, Ti–Ni SMAs are considered the most successful smart materials for commercial applications [4]. However, due to the limitation of phase transition temperature, this type of SMAs cannot be used under high temperature conditions. Therefore, in order to solve this problem, a large number of high temperature SMAs have been studied, such as Ti–Ni–(Hf/Zr/Pt/Pd) [5–8], Ni–Mn–Ga [9], Zr–Cu [10] and Cu–Al–Fe [11] SMAs, etc. Among them, the phase transition temperature (PTT) of Cu–Al–Fe SMAs can not only reach 573 K, but also are cheap and easy to process, and have been widely studied [12–14].

As is known to all, due to the brittleness and poor thermal stability of Cu–Al-based SMAs, the SME decreases sharply [15]. The reason for high brittleness is the existence of a

brittle precipitate phase γ with the structural characteristics of Cu₉Al₄ at grain boundaries [16]. In addition, the PTT and SME of Cu–Al-based SMAs are closely related to the content of Al as well as the content of the third element, that is, to the structure and type of martensite [17–19]. This is due to the change of the valence electron by atom (e/a), which affects the range of PTT [20–24]. For example, Recarte et al. [25] found through research that with the increase of Al content, the martensite structure of Cu–Al–Ni SMAs gradually changed from β' martensite to γ' martensite. Chen et al. [26] found that with the increase of Al content, the SME of Cu–Al–Ga SMAs is gradually enhanced. Aydoğdu et al. [27] found that with the increase of Co content, the martensite of Cu–Al–Co SMAs gradually widens and precipitated phase is formed. Silva et al. [28, 29] found that Ag could effectively reduce the β' phase decomposition reaction rate. However, Cu–Al–Fe SMAs, as a new high-temperature Cu–Al-based SMAs, have relatively little basic research in this respect [30].

Therefore, Cu–Al–Fe SMAs are systematically reported in this paper. The effects of Al content and heat treatment on microstructure, thermal stability, PTT, SME and mechanical properties were investigated. This work has important

✉ Jiaying Jian
jianjiaying@xatu.edu.cn

¹ School of Materials and Chemical Engineering, Xi'an Technological University, Xi'an 710021, China

implications for material design and performance optimization, thus promoting the applicability of Cu–Al–Fe SMAs.

Materials and methods

$\text{Cu}_{95-x}\text{Al}_x\text{Fe}_5$ ($x = 11, 12, 13$ mass%) SMAs were fabricated from the raw materials of pure Fe (purity: 99.9%, Tijo, China), Al (purity: 99.99%, Tijo, China) and Cu (purity: 99.9%, Tijo, China). Each sample masses 30 g and was remelted 6 times to obtain as-cast sample with chemical homogeneity by arc-melting under an Ar atmosphere. And $\text{CuAl}_{11}\text{Fe}_5$ SMAs, $\text{CuAl}_{12}\text{Fe}_5$ SMAs and $\text{CuAl}_{13}\text{Fe}_5$ SMAs in the as cast state were named ZC-1, ZC-2 and ZC-3, respectively. Subsequently, the quenching process of $\text{Cu}_{95-x}\text{Al}_x\text{Fe}_5$ ($x = 11, 12, 13$ mass%) SMAs were annealed at 1173 K for 24 h, followed by water quenching. And $\text{Cu}_{84}\text{Al}_{11}\text{Fe}_5$ SMAs, $\text{Cu}_{83}\text{Al}_{12}\text{Fe}_5$ SMAs and $\text{CuAl}_{13}\text{Fe}_5$ SMAs in the quenched state were named QC-1, QC-2 and QC-3, respectively.

The phase analysis of these samples was detected using an X-ray diffractometer (XRD, 40 kV, 30 mA and 4°min^{-1} , Bruker D2, Germany). The surface morphologies of these samples were found by scanning electron microscopy (SEM, MIRA3 XMU, Czech) and optical microscopy (OM, EPIPHOT300U, Japan). Moreover, the chemical composition of these samples was determined by energy dispersive X-ray spectrometer (EDS). The PTT and thermal cycle stability were determined by using differential scanning calorimeter (DSC, DSC823e-*0303022601, Switzerland), and the rate of heating and cooling during heating and cooling was 2 K min^{-1} . The cylindrical sample ($\Phi 4 \text{ mm} \times 4 \text{ mm}$) was cut from the parts, and the compression tests were carried out by universal tensile testing machine (SANS, China). The shape memory effect was tested using the dimensional variation of the samples. The length of these samples was estimated before loading (h_0), after unloading (h_1), after heating to 873 K for 3 min and after air cooled to room temperature to restore shape (h_2). Among them, the heating process was

completed by a thermomechanical analyzer (TMA, TMA/SDT840, Switzerland). The shape recovery strain and ratio after heating were calculated as:

$$\varepsilon_{\text{SME}} = \left(\frac{h_2 - h_1}{h_0} \right) \times 100\% \quad (1)$$

$$f_{\text{SME}} = \left(\frac{h_2 - h_1}{h_0 - h_1} \right) \times 100\% \quad (2)$$

Results and discussion

Figure 1 shows the X-ray diffraction patterns of $\text{Cu}_{95-x}\text{Al}_x\text{Fe}_5$ ($x = 11, 12, 13$ mass%) SMAs in the as-cast and quenched states, respectively. The diffraction peaks of β' martensite and γ' martensite can be observed in Fig. 1, and the martensite diffraction peaks of all SMAs expect QC-3 are β' martensite, while the martensite diffraction peaks of QC-3 are composed of β' and γ' . According to the results, when the content of Al is high, the martensite will change from β' to γ' during quenching, while when the content of Al is low, the martensite structure will not change. It is worth noting that the main diffraction peak of β' martensite of QC-1 is about 44° ; when the Al content increases to 12, the main diffraction peak of QC-2 moves to the right near 47° , but it is still the diffraction peak of β' martensite; When the Al content is further increased to 13, the diffraction peak of QC-3 near 72° is significantly enhanced, while the diffraction peak near 47.2° is significantly weakened, at the time, the main diffraction peak also changes from is β' martensite to γ' martensite.

In addition, the diffraction peaks of Fe(Cu, Al) and α (Cu) phases are present in ZC-1, while only Fe(Cu, Al) phase is in other as-cast alloys. However, neither of these two phases exist in all alloys after quenching. In summary, with the increase of Al content, α (Cu) phase gradually disappeared and martensite content gradually increased. In addition,

Fig. 1 The X-ray diffraction patterns of $\text{Cu}_{95-x}\text{Al}_x\text{Fe}_5$ ($x = 11, 12, 13$ mass%) SMAs in the as-cast and quenched states. **a** the as-cast state; **b** the quenched state

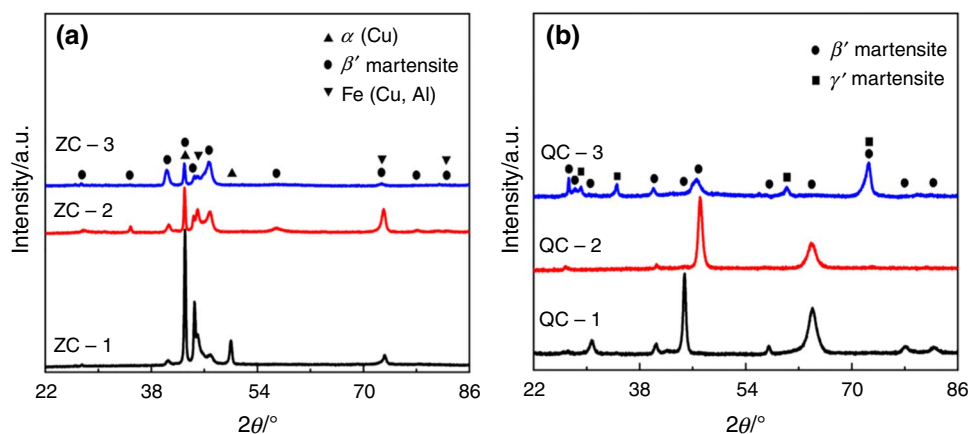


Fig. 2 The OM (a–c) and SEM (d–f) images of $\text{Cu}_{95-x}\text{Al}_x\text{Fe}_5$ ($x = 11, 12, 13$ mass%) SMAs in the as-cast state. **a** and **d** ZC-1; **b** and **e** ZC-2; **c** and **f** ZC-3

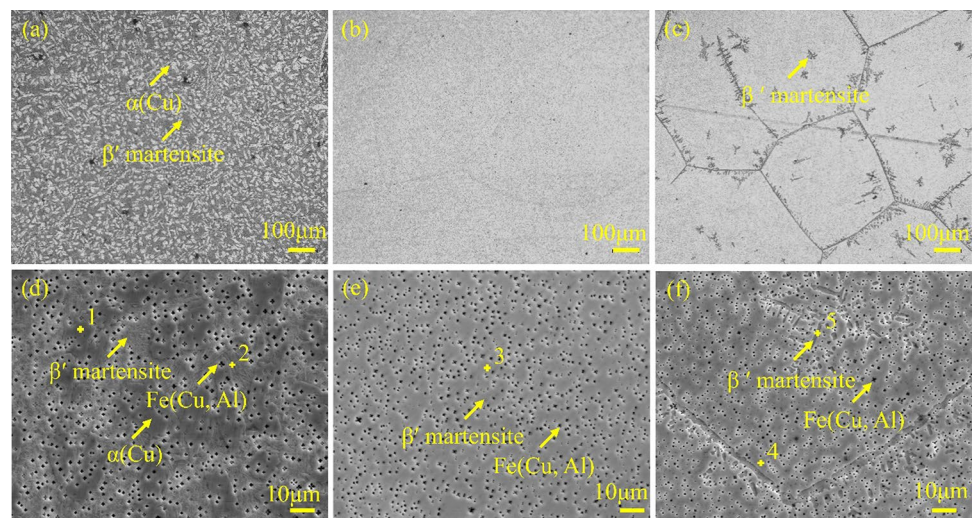
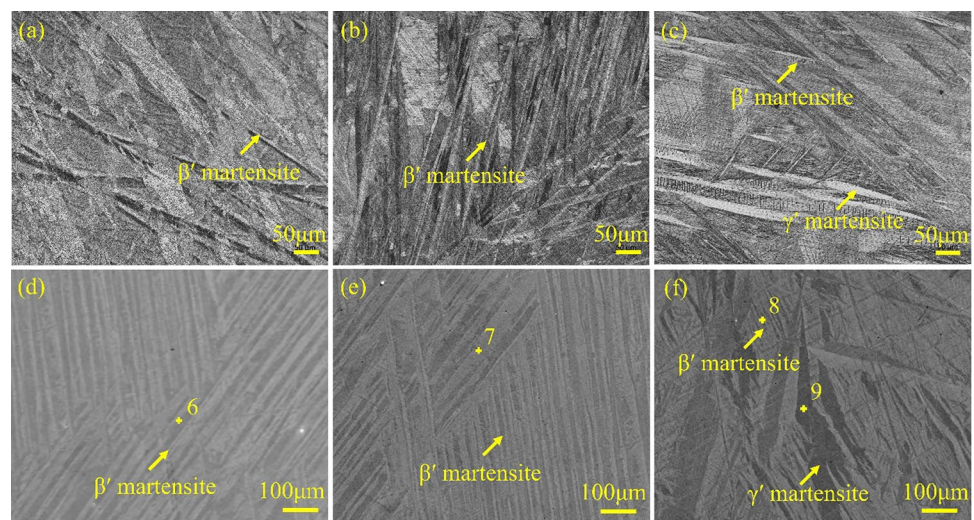


Fig. 3 The OM (a–c) and SEM (d–f) images of $\text{Cu}_{95-x}\text{Al}_x\text{Fe}_5$ ($x = 11, 12, 13$ mass%) SMAs in the quenched state. **a** and **d** QC-1; **b** and **e** QC-2; **c** and **f** QC-3



when the alloy is quenched, due to the increase of cooling rate, the solid solubility increases, resulting in the Fe element does not precipitate, so only the diffraction peak of martensite is found. The change of structure and morphology would be further studied in the following work.

Figures 2 and 3 show the OM and SEM images of $\text{Cu}_{95-x}\text{Al}_x\text{Fe}_5$ ($x = 11, 12, 13$ mass%) SMAs in the as-cast and quenched states, respectively. The chemical composition was determined by EDS, as shown in Table 1. In this paper, two kinds of martensite produced are γ' type and β' type, which will be identified by the subsequent results. For the as-cast state, it can be seen from Fig. 2 and Table 2 that ZC-2 and ZC-3 are mainly composed of β' type martensite, while ZC-1 is mainly composed of β' martensite and $\alpha(\text{Cu})$ phase. This is due to the fact that with the decrease of Al content, martensite cannot be completely formed, resulting in the existing of $\alpha(\text{Cu})$ phase. In addition, the snowflake-shaped $\text{Fe}(\text{Cu}, \text{Al})$ phase is detected in all alloys. For the quenched state, combined with Fig. 3 and Table 2, it can be seen that

QC-1 and QC-2 are mainly composed of β' martensite, while QC-3 not only found β' martensite, but also found thicker γ' type martensite. Additionally, there is no $\text{Fe}(\text{Cu}, \text{Al})$ phase in all quenched alloys, due to the increase in solid solubility caused by quenching, which results in the full dissolution of the Fe element into the matrix. On this basis, it can be found that the main reason leading to the gradual transformation of β' martensite to γ' martensite is the increase of electron concentration with the increase of Al content [23]. These results are consistent with those of X-ray diffraction.

Figure 4 exhibits the thermal cycle curves of $\text{Cu}_{95-x}\text{Al}_x\text{Fe}_5$ ($x = 11, 12, 13$ mass%) SMAs in the as cast state, and the data of their first measured PTT are shown in Table 2. It can be seen that PPT of SMAs is very sensitive to fluctuation of Al content. And the austenite transition start temperature (A_s) and martensite transition start temperature (M_s) of $\text{Cu}_{95-x}\text{Al}_x\text{Fe}_5$ ($x = 11, 12, 13$ mass%) SMAs first increase and then decrease with the decrease of Al content. At the same time, it can be seen from Table 2 that A_s and M_s of

Table 1 EDS results from points of 1–9

Sample	Point	Cu		Al		Fe	
		Mass/%	Atomic/%	Mass/%	Atomic/%	Mass/%	Atomic/%
ZC-1	1	86.78	78.62	7.03	15.00	6.19	6.38
	2	84.68	72.38	12.24	24.63	3.08	3.00
ZC-2	3	83.23	70.41	13.07	26.03	3.70	3.56
ZC-3	4	85.85	73.84	12.16	24.53	1.99	1.94
	5	82.54	69.81	13.00	25.89	4.47	4.30
QC-1	6	80.34	67.22	13.76	27.12	5.94	5.66
QC-2	7	81.33	68.62	13.11	26.04	5.56	5.34
QC-3	8	83.73	71.04	12.84	25.64	3.44	3.32
	9	80.09	65.89	15.45	29.94	4.45	4.17

Table 2 The PTT of all alloy

PTT	ZC-1	ZC-2	ZC-3	QC-1	QC-2	QC-3
M_s/K	455	510	485	505	509	484
A_s/K	600	620	613	580	617	592

ZC-1 are 600 K and 455 K, respectively. When Al content increases by 1 mass%, them of ZC-2 increase by 20 K and 55 K, respectively. However, when the Al content is further increased to 13 mass%, them of ZC-3 decrease by 7 K and 25 K, respectively. According to the analysis results, since both ZC-1 and ZC-3 contain needle-like β' martensite, while ZC-2 contains plane-like β' martensite, the M_s and A_s of needle-like β' martensite is significantly lower than that of plane-like β' martensite. In addition, due to ZC-1 contains a large amount of $\alpha(\text{Cu})$ phase, the M_s and A_s is lower than ZC-3, so it can be seen that the more needle-like β' martensite contains, the higher the PPT.

It can be seen from Fig. 4 that after 15 thermal cycles, the phase transition types of ZC-1, ZC-2 and ZC-3 do not change significantly, but the width and location of phase transition peaks do. After 15 thermal cycles of ZC-1, The difference of temperature of the peak austenite transition (A_p) and martensite transition (M_p) is 30 K and 15 K, respectively. When the content of Al is 12 mass%, the difference of A_p remains unchanged, while the difference of M_p increases to 63 K. When Al content is 13 mass%, the difference of A_p and M_p decrease by 3 K and 2 K, respectively. According to the results, the A_p and M_p of needle-like β' martensite is more stable than that of plane-like β' martensite, and the stability is better with more needle-like β' martensite content. Figure 4g–i show the relationship between the enthalpy of phase transition and the number of cycles of $\text{Cu}_{95-x}\text{Al}_x\text{Fe}_5$ ($x = 11, 12, 13$ mass%) SMAs. By fitting the data, the relationship between enthalpy and cycle number in the process of endothermic and exothermic of ZC-1, ZC-2 and ZC-3 can be obtained as follows:

$$y = -15.36 + 1.22x - 0.04x^2 \quad (3)$$

$$y = -8.01 + 0.96x - 0.04x^2 \quad (4)$$

$$y = -46.35 + 2.23x - 0.09x^2 \quad (5)$$

$$y = -32.34 + 2.54x - 0.08x^2 \quad (6)$$

$$y = -44.16 + 0.08x - 0.005x^2 \quad (7)$$

$$y = -28.35 + 0.16x - 0.004x^2 \quad (8)$$

where x and y denote cycle number and enthalpy. It can be seen that the thermal stability of needle-like β' martensite is better than that of plane-like β' martensite, and the more needle-like β' martensite content, the better thermal stability.

Figure 5 exhibits the thermal cycle curves of $\text{Cu}_{95-x}\text{Al}_x\text{Fe}_5$ ($x = 11, 12, 13$ mass%) SMAs in the quenched state, and the data of their first measured PTT are shown in Table 2. It can be seen that PPT of SMAs is very sensitive to fluctuation of Al content. And the austenite transition start temperature (A_s) and martensite transition start temperature (M_s) of $\text{Cu}_{95-x}\text{Al}_x\text{Fe}_5$ ($x = 11, 12, 13$ mass%) SMAs in the quenched state first increase and then decrease with the decrease of Al content. At the same time, it can be seen from Table 2 that A_s and M_s of QC-1 are 580 K and 505 K, respectively. When Al content increases by 1 mass%, them of QC-2 increase by 37 K and 4 K, respectively. However, when the Al content is further increased to 13 mass%, them of QC-3 decrease by 25 K and 25 K, respectively. The results show that the higher the content of needle-like β' martensite is, the higher the

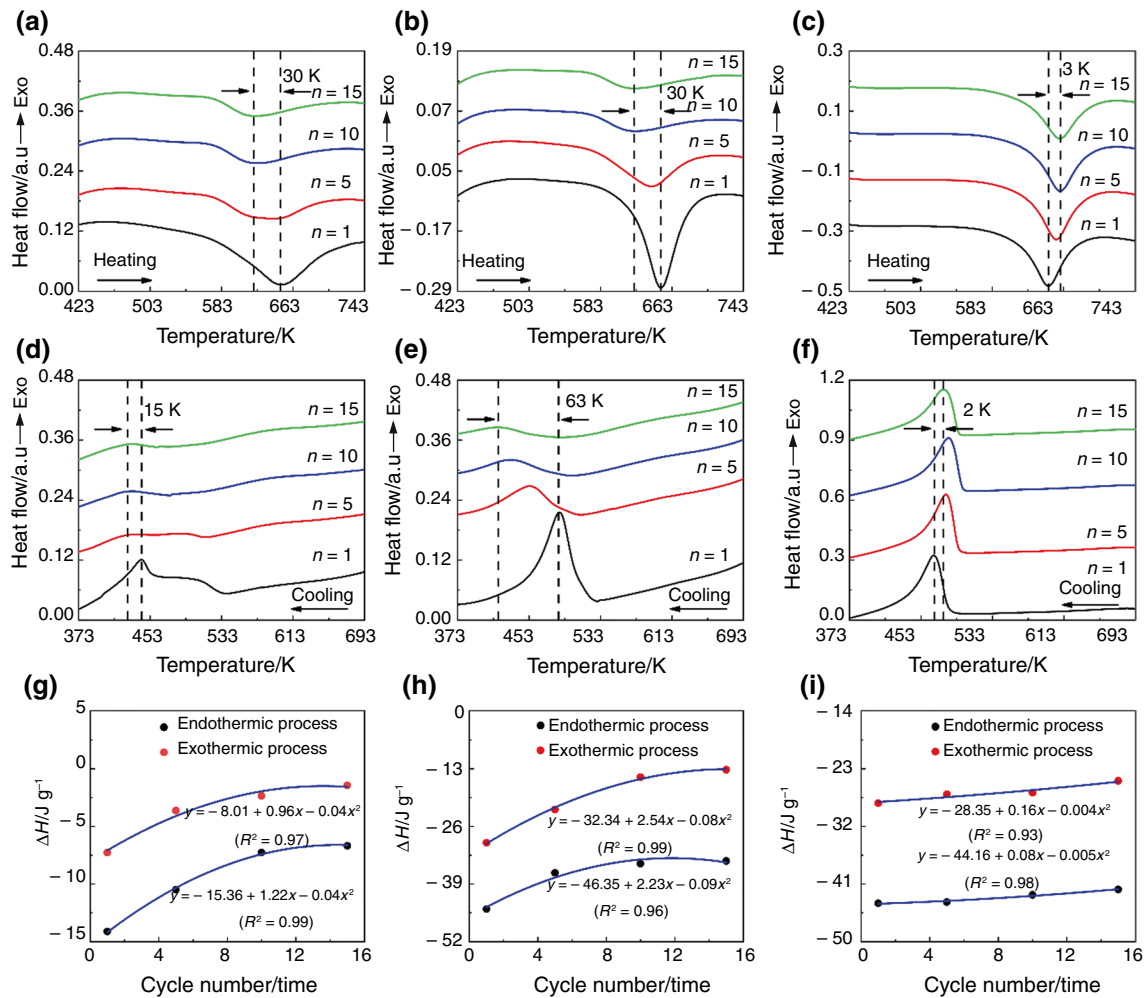


Fig. 4 Thermal cycle curves of $\text{Cu}_{95-x}\text{Al}_x\text{Fe}_5$ ($x = 11, 12, 13$ mass%) SMAs in the as cast state. **a, d** and **g** ZC-1; **b, e** and **h** ZC-2; **c, f** and **i** ZC-3

PPT is. In addition, plate-like γ' martensite has a lower austenite transition temperature than needle-like β' martensite, and only a lower temperature is needed to achieve austenite–martensite transition.

It can be seen from Fig. 5 that after 15 thermal cycles, the phase transition types of QC-1 and QC-2 do not change significantly, while the phase transition type of QC-3 changes significantly. In addition, the width and location of phase transition peaks change. After 15 thermal cycles of QC-1, The difference of the temperature of the peak austenite transition (A_p) and martensite transition (M_p) is 4 K and 46 K, respectively. When the content of Al is 12 mass%, the difference of A_p increases to 19 K, while the difference of M_p decreases to 42 K. When the Al content is further increased to 13 mass%, the difference of A_p is further increased to 37 K, while the difference of M_p is further reduced to 7 K. According to the results, with the increase of the number of cycles, the two-step phase transition of QC-3 in the endothermic process is transformed into a one-step phase

transition, which indicates that with the increase of the number of cycles, the γ' martensite disappears and only a single β' martensite exists. Figure 5g–i show the relationship between the enthalpy of phase transition and the number of cycles of $\text{Cu}_{95-x}\text{Al}_x\text{Fe}_5$ ($x = 11, 12, 13$ mass%) SMAs. By fitting the data, the relationship between enthalpy and cycle number in the process of endothermic and exothermic of QC-1, QC-2 and QC-3 can be obtained as follows:

$$y = -52.19 + 0.39x + 0.005x^2 \quad (9)$$

$$y = -21.11 + 1.25x - 0.05x^2 \quad (10)$$

$$y = -52.19 + 0.39x - 0.05x^2 \quad (11)$$

$$y = -21.11 + 1.25x - 0.05x^2 \quad (12)$$

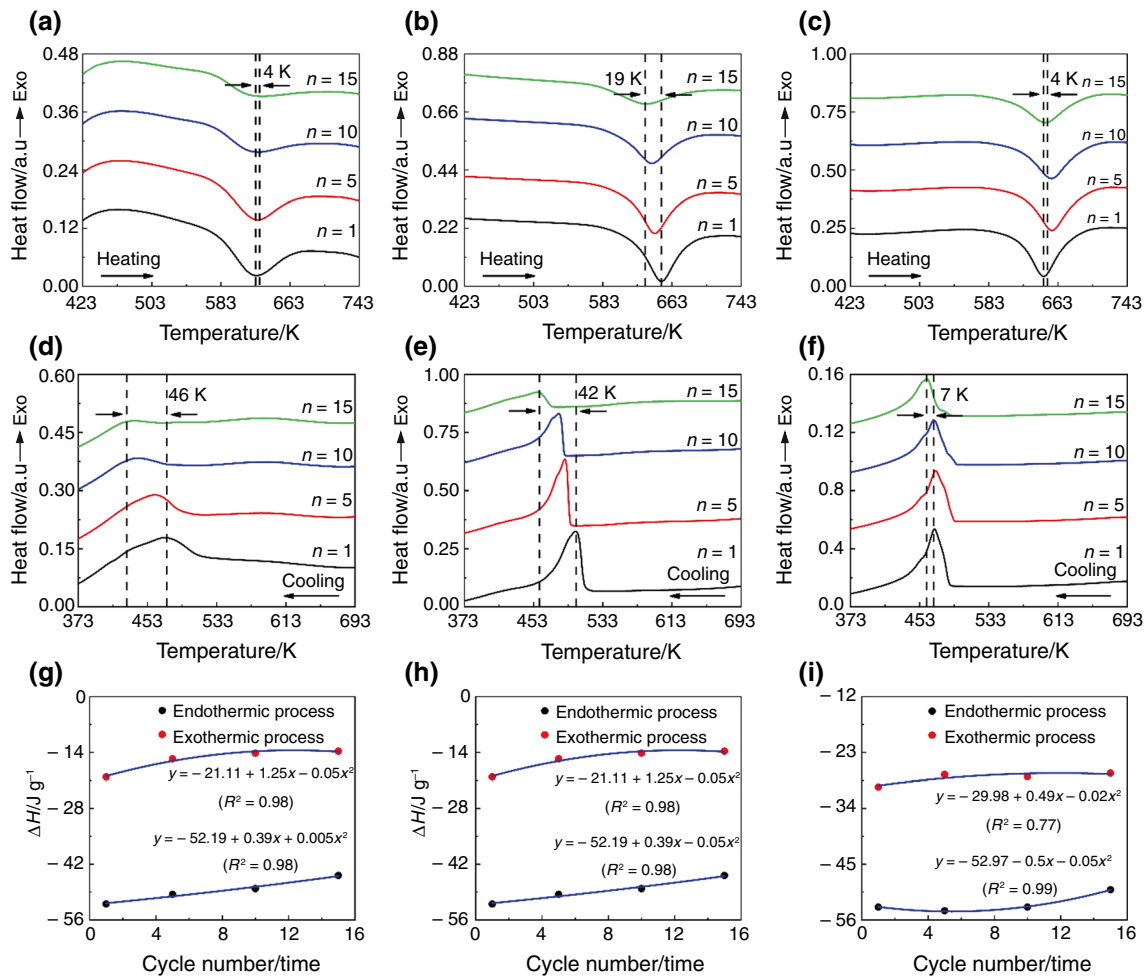


Fig. 5 Thermal cycle curves of $\text{Cu}_{95-x}\text{Al}_x\text{Fe}_5$ ($x = 11, 12, 13$ mass%) SMAs in the quenched state. **a, d** and **g** QC-1; **b, e** and **h** QC-2; **c, f** and **i** QC-3

$$y = -52.97 - 0.5x - 0.05x^2 \quad (13)$$

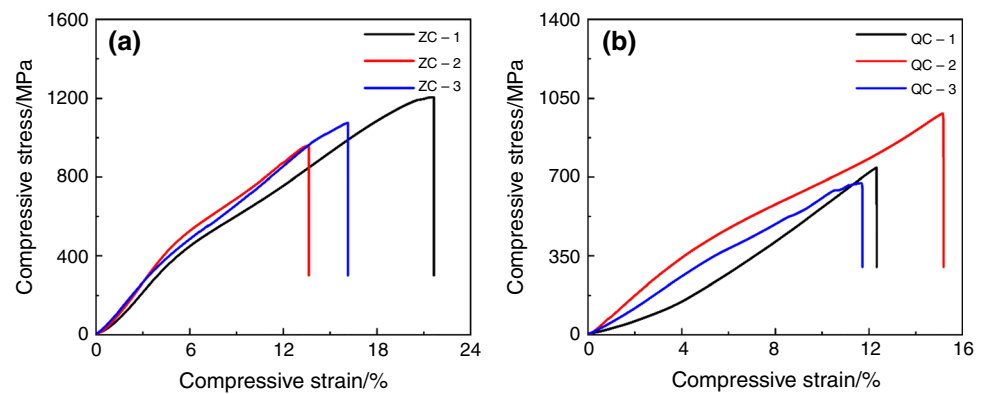
$$y = -29.98 + 0.49x - 0.02x^2 \quad (14)$$

where x and y denote cycle number and enthalpy. It can be seen that the thermal stability of β' martensite is better than that of γ' martensite, and compared with the cast state, the thermal stability after heat treatment is better.

Figure 6 exhibits the compressive strain and stress curves of $\text{Cu}_{95-x}\text{Al}_x\text{Fe}_5$ ($x = 11, 12, 13$ mass%) SMAs in the as-cast and quenched states. For the as-cast state, the compressive stresses and strains were scaled to be 1205.4 MPa and 21.7% for ZC-1; 959.3 MPa and 13.6% for ZC-2; 1075.1 MPa and 16.1% for ZC-3, respectively. It can be found that the compressive strength and strain first decrease and then increase with the increasing Al content. The result indicates that ZC-1 has the best compressive stress and strain, which is due to the presence of a large amount of $\alpha(\text{Cu})$ phase in the

alloy. When the increasing Al content, the $\alpha(\text{Cu})$ phase with excellent mechanical properties disappears, resulting in a decrease in mechanical properties. However, with the further increasing Al content, a large number of needle-like β' martensite is formed, which improved the mechanical properties. For the quenched state, the compressive stresses and strains were scaled to be 742.7 MPa and 12.3% for ZC-1; 987.6 MPa and 15.2% for ZC-2; 675.8 MPa and 11.7% for ZC-3, respectively. It can be seen that the compressive stress and strain first increase and then decrease with the increasing Al content. This is due to the fact that when the Al content is increased to 12, the structure consists of a single needle-like β' martensite, thereby improving the mechanical properties, but when the Al content is further increased, a thicker plate-like γ' martensite is formed, resulting in a decrease in mechanical properties. In summary, compared with the three phases, $\alpha(\text{Cu})$ phase has the best compressive stress and strain, followed by β' martensite, and γ' martensite has the worst.

Fig. 6 The compressive strain–stress curves of $\text{Cu}_{95-x}\text{Al}_x\text{Fe}_5$ ($x = 11, 12, 13$ mass%) SMAs in **a** cast and **b** quenched states. **a** the as-cast state; **b** the quenched state



In order to study the SME of $\text{Cu}_{95-x}\text{Al}_x\text{Fe}_5$ ($x = 11, 12, 13$ mass%) SMAs in the as-cast and quenched states, the samples were compressed to 5% pre-strain, as shown in Fig. 7a and b. The recovery curves were given in Fig. 7c and d. In addition, all residual strains, recovery strains and recovery ratios are shown in Table 3. It can be seen from Fig. 7 and Table 3 that the SME of the studied alloy is different in different states. In the as-cast state, the recovery strain and recovery ratio gradually increase with the increase of Al content, and the recovery strain and recovery ratio of ZC-3 are the largest, which are 0.61% and 64.21%, respectively. This is due to the existence of a large number of $\alpha(\text{Cu})$ phases without SME in ZC-1, resulting in poor SME; with

the increase of Al content, the $\alpha(\text{Cu})$ phase in ZC-2 disappeared, which effectively improved the SME; with the further increase of Al content, the SME is further improved due to the presence of a large number of needle-like β' martensite in ZC-3. In addition to this, the recovery strain and recovery ratio first increase and then decrease with the increase of Al content in the quenched state. The main reason is that when the Al content increase to 12 mass%, the microstructure of QC-2 is a single needle-like β' martensite, so it has a good SME; however, with the further increase of Al content, the SME is weakened, which is due to the formation of plate-like γ' martensite in QC-3. In summary, compared

Fig. 7 The compressive curves with a pre-strain of 5% and length–temperature curves of $\text{Cu}_{95-x}\text{Al}_x\text{Fe}_5$ ($x = 11, 12, 13$ mass%) SMAs under the as-cast and quenched states. **a** and **c** the as-cast state; **b** and **d** the quenched state

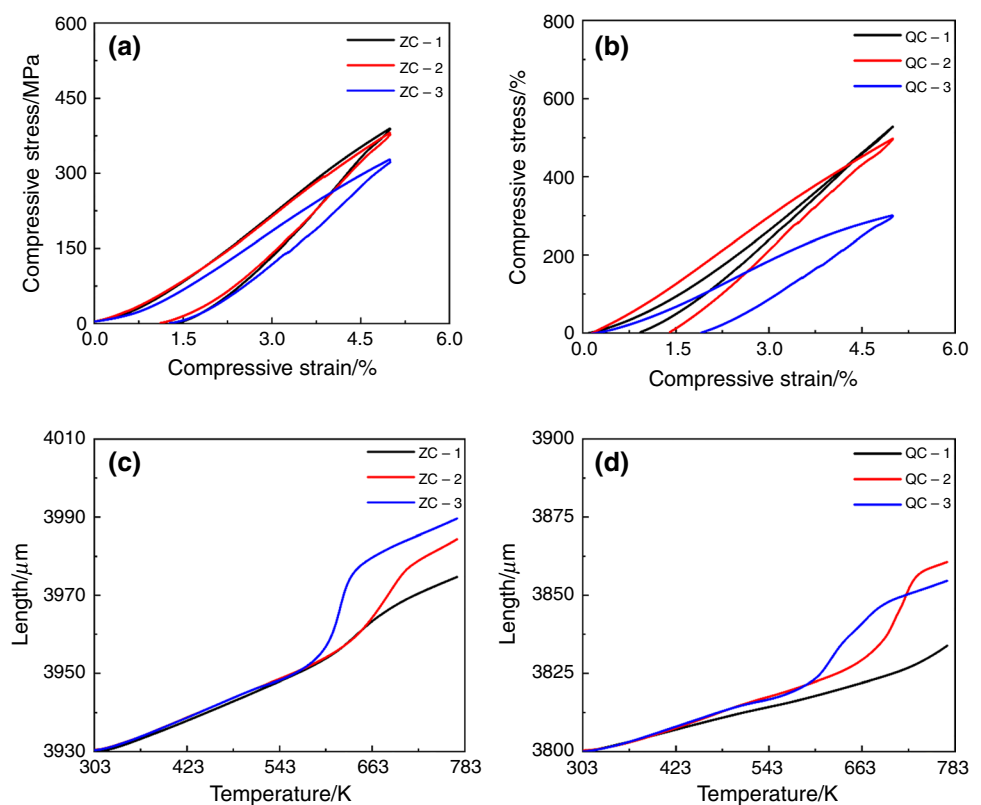


Table 3 The SME of 5% pre-strain

Sample	Residual strain/%	Recovery strain/%	Recovery ratio/%
ZC-1	0.97	0.25	25.77
ZC-2	0.98	0.47	47.96
ZC-3	0.95	0.61	64.21
QC-1	0.84	0.54	64.29
QC-2	0.96	0.81	84.38
QC-3	1.27	0.62	48.82

with plate-like γ' martensite, needle-like β' martensite has the best SME.

Conclusions

In this paper, the microstructure, PPT, SME, thermal stability and compressive mechanical properties of $\text{Cu}_{95-x}\text{Al}_x\text{Fe}_5$ ($x = 11, 12, 13$ mass%) SMAs in the as-cast and quenched states were researched. The main findings and conclusions can be summarized as follows:

1. The microstructure of ZC-1 is a mixture of $\alpha(\text{Cu})$ phase, β' martensite and $\text{Fe}(\text{Cu}, \text{Al})$ phase, and with the increase of Al content, the $\alpha(\text{Cu})$ phase in the microstructure of ZC-2 and ZC-3 disappear into a mixture of β' martensite and $\text{Fe}(\text{Cu}, \text{Al})$ phase. After quenching, Fe metal is completely soluble in the matrix, and the microstructure of QC-1 and QC-2 is a single β' martensite. While the microstructure of QC-3 is a mixture of β' martensite and γ' martensite due to the relatively high Al content.
2. The A_s temperatures of all investigated alloys are greater than 573 K. In addition, the QC-3 undergoes a two-step phase transition during the heating process, which is caused by the presence of two martensite structure and the PTT of γ' martensite is higher than that of β' martensite. The thermal stability of β' martensite is better than that of γ' martensite, and compared with the as-cast alloy, the thermal stability of quenched alloy is better, so QC-2 has the best thermal stability.
3. The compressive stress and strain of $\text{Cu}_{95-x}\text{Al}_x\text{Fe}_5$ ($x = 11, 12, 13$ mass%) SMAs first decrease and then increase with increasing Al content in the as-cast state, resulting from the decrease of $\alpha(\text{Cu})$ phase, and increase of Al content in β' martensite. However, the compressive stress and strain first increase and then decrease with increasing of Al content in the quenched state, which is caused by the formation of γ' martensite.
4. The recovery strain and recovery ratio remarkably increase with increasing Al content in the as-cast state,

resulting from the increase of β' martensite. However, the recovery strain and recovery ratio first increase and then decrease with increasing Al content in the quenched state, which is due to the formation of γ' martensite. And QC-2 has the best recovery strain and recovery ratio, reaching 0.81% and 84.38%, respectively.

Acknowledgements The current work was funded by the National Natural Science Foundation of China (Grant number: 62204197), Shaanxi Provincial Department of Education (Grant No: 22JK0408), Shaanxi Provincial Science and Technology Department (Grant No: 2023KJXX-149).

Author contributions Yunpeng Gao: writing—original draft, data curation, methodology, conceptualization, formal analysis. Jiaying Jian: writing—review & editing, conceptualization, supervision, methodology, formal analysis, funding acquisition. Zengyun Jian: writing—review & editing.

Data availability Data will be made available on request.

Declarations

Conflict of interest The author declares none conflict of interest.

References

1. Bağ Ö, Ergen S, Yilmaz F, Kölemen U. Influence of Al content on transformation temperature and activation energy of Ti–V–Al high temperature shape memory alloys. *Solid State Commun.* 2021;323: 114104.
2. Tan LC, Tian XH, Gui TL, Cai W. Elastic property and electronic structure of TiNiPt high-temperature shape memory alloys. *Solid State Commun.* 2008;147:8–10.
3. Liang XL, Chen Y, Shen HM, Zhang ZF, Li W, Wang YN. Thermal cycling stability and two-way shape memory effect of Ni–Cu–Ti–Hf alloys. *Solid State Commun.* 2001;119:381–5.
4. Akamine H, Kalbekov A, Higashizono T, Matsuda M, Hata S, Nishida M. Hydrogen-induced phase with martensitic-like characteristics in Ti–Ni shape memory alloys. *J Alloy Compd.* 2023;964: 171470.
5. Zhang C, Xue L, Pestka SA, Ranaiefar M, Atli KC, Honarmandi P, Arróyave R, Karaman I, Elwany A. Processing parameters and martensitic phase transformation relationships in near defect-free additively manufacturing NiTiHf high temperature shape memory alloys. *Mater Design.* 2022;222: 110988.
6. Karakoc O, Atli KC, Benafan O, Noebe RD, Karaman I. Actuation fatigue performance of NiTiZr and comparison to NiTiHf high temperature shape memory alloys. *Mat Sci Eng A-struct.* 2022;829: 142154.
7. Rehman SU, Khan M, Khan AN, Alam K, Jaffery SHI, Ali L, Khan A. Influence of Cu addition on transformation temperatures and thermal stability of TiNiPd high temperature shape memory alloys. *Proc Inst Mech Eng Part L J Mater Des Appl.* 2017;233:800–8.
8. Lin B, Gall K, Maier HJ, Waldron R. Structure and thermomechanical behavior of NiTiPt shape memory alloy wires. *Acta Mater.* 2009;5:257–67.
9. Chiu WT, Goto A, Tahara M, Inamura T, Hosoda H. Effects of volume fraction between single crystal Ni–Mn–Ga ferromagnetic

- shape memory alloy and silicone rubber on the martensite variant reorientation. *J Alloy Compd.* 2022;926: 166862.
10. Yang YX, Deng MQ, Gao WH, Sun B, Fu YD, Meng XL. Enhancing the thermal stability and recoverability of ZrCu-based shape memory alloys via interstitial doping. *Mat Sci Eng A-struct.* 2024;889: 145860.
 11. Dharmendra C, Gururaj K, Pradeep KG, Mohammadi M. Characterization of κ -precipitates in wire-arc additive manufactured nickel aluminum bronze: a combined transmission Kikuchi diffraction and atom probe tomography study. *Addit Manuf.* 2021;46: 102137.
 12. Wang HY, Huang JL, Chen S, Yuan XM, Zhu J, Xu D, Mao JZ. Microstructure and shape memory properties of Cu–Al–Fe alloys with different Al contents made by additive manufacturing technology. *Mater Res Express.* 2022;9: 095701.
 13. Yildiz K, Balci E, Akpınar S. Quenching media effects on martensitic transformation, thermodynamic and structural properties of Cu–Al–Fe–Ti high-temperature shape memory alloy. *J Therm Anal Calorim.* 2017;129:937–45.
 14. Yang SY, Su Y, Wang CP, Liu XJ. Microstructure and properties of Cu–Al–Fe high-temperature shape memory alloys. *Mat Sci Eng B Adv.* 2014;185:67–73.
 15. Raju TN, Sampath V. Influence of aluminium and iron contents on the transformation temperatures of Cu–Al–Fe shape memory alloys. *Trans Indian Inst Met.* 2011;64:165–8.
 16. Abolhasani D, Moon B, Kang N, VanTyne CJ, Moon YH. High-temperature Cu–Al shape memory alloy in ternary combination with graphene fabricated by powder bed fusion process. *J Alloy Compd.* 2023;960: 170707.
 17. López-Ferreño I, Gómez-Cortés JF, Breczewski T, Ruiz-Larrea I, Nó ML, Juan JMS. High-temperature shape memory alloys based on the Cu–Al–Ni system: design and thermomechanical characterization. *J Mater Res Technol.* 2020;9:9972–84.
 18. Silva ÍJA, Silva DDS, Lima BASG, Feitosa FRP, Brito ICA, Caluête RE, Gome RM, Oliveira DF. Study of the thermodynamic parameters, microstructure and mechanical properties of a CuAlNi shape memory alloy produced with recycled aluminum. *Mater Today Commun.* 2023;36: 106527.
 19. Cai L, Wang YN, Huang W, He W, Peng HB, Wen YH. Effect of Ni alloying on vacancy behavior and damping capacity in martensitic ductile Cu–Al–Mn alloys. *J Mater Res Technol.* 2023;25:7109–18.
 20. Bachaga T, Daly R, Escoda L, Sunol JJ, Khitouni M. Influence of chemical composition on martensitic transformation of MnNiIn shape memory alloys. *J Therm Anal Calorim.* 2015;122:167–73.
 21. Bachaga T, Rekek H, Krifa M, Suñol JJ, Khitouni M. Investigation of the enthalpy/entropy variation and structure of Ni–Mn–Sn (Co, In) melt-spun alloys. *J Therm Anal Calorim.* 2016;126:1463–8.
 22. Bachaga T, Ren W, Sunol JJ, Jing C. Microstructure characterization, structure and magnetic properties of Ni–Mn–Sn shape memory alloys. *J Therm Anal Calorim.* 2022;147:2147–2154.
 23. Bachaga T, Zhang J, Khitouni M, Sunol JJ. NiMn-based Heusler magnetic shape memory alloy: a review. *Int J Adv Manuf Technol.* 2019;103:2761–2772.
 24. Bachaga T, Daly R, Suñol JJ, Saurina J, Escoda L, Legarreta LG, Hernando B, Khitouni M. Effects of Co additions on the martensitic transformation and magnetic properties of Ni–Mn–Sn shape memory alloys. *J Therm Anal Calorim.* 2015;28:3087–92.
 25. Recarte V, Pérez-SáEZ RB, Bocanegra EH, Nó ML, Juan JS. Influence of Al and Ni concentration on the martensitic transformation in Cu–Al–Ni shape-memory alloys. *Metall Mater Trans A.* 2002;33:2581–91.
 26. Chen SS, Chen XQ, Guo LP, Zheng SW, Chen F, Wang CP, Yang SY. Microstructure, martensitic transformation and shape effect of novel Cu–Al–Ga based shape memory single crystals. *Vacuum.* 2023;210: 111824.
 27. Aydoğdu Y, Kürüm F, Kök M, Yakinci ZD, Aydoğdu A. Thermal properties, microstructure and microhardness of Cu–Al–Co shape memory alloy system. *Trans Indian Inst Met.* 2014;67:595–600.
 28. Silva RAG, Adorno AT, Magdalena AG, Carvalho TM, Stipcich M, Cuniberti A, Castro ML. Thermal behavior of the Cu-22.55 at.% Al alloy with small Ag additions. *J Therm Anal Calorim.* 2011;103:459–63.
 29. Silva RAG, Machado ES, Adorno AT, Magdalena AG, Carvalho TM. Completeness of β -phase decomposition reaction in Cu–Al–Ag alloys. *J Therm Anal Calorim.* 2012;109:927–31.
 30. Ge Y, Vronka M, Veřtát P, Karlík M, Hannula SP, Heczko O. Deformation twinning with different twin-boundary mobility in 2H martensite in Cu–Ni–Al shape memory alloy. *Acta Mater.* 2022;226: 117598.

Publisher's Note Springer Nature remains neutral with regard to jurisdictional claims in published maps and institutional affiliations.

Springer Nature or its licensor (e.g. a society or other partner) holds exclusive rights to this article under a publishing agreement with the author(s) or other rightsholder(s); author self-archiving of the accepted manuscript version of this article is solely governed by the terms of such publishing agreement and applicable law.